Reversible and Irreversible Structural Changes in Cu/ZnO/ZrO_2 Catalysts during Methanol Synthesis

Lucas Warmuth,*,⊥ Matthias Steurer,⊥ Dieter Schild, Anna Zimina, Jan-Dierk Grunwaldt, and Stephan Pitter

ABSTRACT: The structure and chemical state of heterogeneous catalysts are closely related to their operational stability. Knowing these relationships as precisely as possible is thus essential for further catalyst development. This work focuses on the deactivation of a Cu/ZnO/ZrO_2-type catalyst for methanol synthesis. Experiments were performed in a parallel setup, with which time-dependent changes in the catalyst material can be observed. Elucidation of potential deactivation pathways is described for catalyst aging at different times on stream (0, 50, 935 h). Data from X-ray absorption spectroscopy, X-ray photoelectron spectroscopy, N_2 physisorption, and transmission electron microscopy measurements reveal that sintering of Cu^0 domains and restructuring within ZnO domains mainly contribute to deactivation. Subsequent reactivation by reduction (in H_2/N_2) reverts the observed structural changes only to a limited extent. Moreover, this work highlights the participation of ZrO_2 as a promoter and reveals redispersion of zirconia after initial reduction.

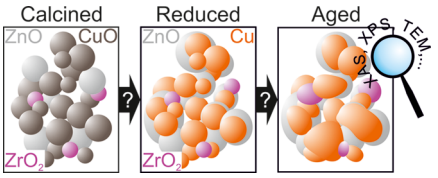

KEYWORDS: *methanol catalysts, copper, zinc, zirconia, catalyst deactivation, EXAFS, XPS, sintering*

INTRODUCTION

Methanol (MeOH) is a widely used platform chemical in the chemical industry and a potential key compound for chemical hydrogen storage and transport.[1−3] On the search for suitable sustainable energy carriers on a global scale, the role of methanol is increasingly in focus as the world's demand intensifies (2015: ≈75 Mt; 2021: ≈110 Mt; 2025 estimate: ≈145 Mt).[4,5] As methanol is produced from syngas (a mixture of H_2, CO, and small amounts of CO_2) by a catalyzed process, the need for efficient and long-term stable catalyst systems arises. This leads to a search for more advanced materials, in particular, based on the Cu/ZnO/Al_2O_3 (CZA) catalysts widely used in industrial applications.[6−8] CO_2-rich feeds and H_2 from solar-based sources (e.g., photovoltaic-assisted electrolysis) can reduce the carbon footprint and contribute to a sustainable methanol synthesis.[9] For CO_2-rich feeds, zirconia outplays alumina as a promoter in terms of productivity and stability, which is assumed to be due to enhanced CO_2 adsorption, electronic, or strong metal support interaction (SMSI) effects.[10−16] However, occurring impurities from the mentioned sources could be a challenge for long-term catalyst usage, as the stability of catalysts is important regarding economic and logistic challenges. In parallel, increased water formation from CO_2-rich syngas feeds can in turn additionally reduce the stability[17,18] of such catalysts as mentioned below. Therefore, the fundamental understanding of respective deactivation phenomena and knowledge-based material improvement is highly desired.

Deactivation of catalysts is widely discussed in the literature, with sintering, coking, and poisoning as the most relevant processes.[19−23] For Cu/ZnO-based catalysts in methanol synthesis, the overall performance is a general but unspecific descriptor of deactivation. However, the performance reduction can be linked to changes in either the structure or the morphology of the material, and it also strongly depends on the syngas feed mixture. With a $H_2/CO/CO_2$ ratio of 4:0:1, the conversion decrease during the initial 50 h ToS was found to be significantly lower than that for the 4:1:0 ratio.[24] Additionally, the CO_2/CO quotient as well as the H_2/CO_x quotient influences the oxidative potential of the syngas feed and hence also influences the oxidation state of active metals (CuZn alloy vs Cu/ZnO_{1-x} vs Cu/ZnO).[25−27] The oxidative environment is often discussed as a detrimental factor inducing structural changes due to oxidation of Cu^0 or Cu^0Zn^0 species with subsequent deactivation.[28] To reveal the structure and oxidation state of Cu in activated/deactivated states, strict anoxic handling of materials for ex situ or operando measurements is to be ensured.[29,30]

Sintering with the loss of (Cu) surface area is the most prominent deactivation process described in the literature: Mainly, deactivation is ascribed to the mobility of reduced Cu^0 nanoparticles and/or also reduced Cu^0Zn^0 species, with the latter assumedly emerging upon overreduction initiated by CO

or H_2 and harsh reduction conditions.[24−27,31,32] A threshold for sintering can be estimated by the Hüttig temperature (approximately 134 °C for Cu; surface mobility only) and the Tamann temperature (approximately 406 °C for Cu; crystal lattice mobility). These temperatures depict the starting points for sintering and were confirmed by in situ extended X-ray absorption fine structure (EXAFS) studies.[33,34] Additionally, nanostructuring can reduce the melting point significantly,[35] and the temperature parameters of sintering processes have to be examined individually for every particular system.

The crystallite growth of ZnO has been observed in a deactivation study during 148 days on CZA. First, an amorphous/graphitic ZnO_x overlayer on Cu^0 particles emerges after catalyst reduction, turning into ZnO with rock salt and wurtzite structure before the subsequent coalescence of Cu^0 particles.[29,30,36]

Coking is assumed to be relevant for harsher conditions only (temperatures >300 °C, under stoichiometric H_2 feed concentration, generally low CO_2 feed concentration).[19,23] Furthermore, additional feed impurities (e.g., chlorine and sulfur species) may lead to active site oxidation and enhance metal migration.[19] Contaminants as Ni and Fe (from metal tubings) can also contribute to catalyst deactivation due to enhanced wax and coke formation.[19]

Conversion of a CO_2-rich syngas feed leads to increased formation of water according to eqs 1 and 2.

$$\Delta H_{298} = -49.1\ \text{kJ mol}^{-1}$$
$$CO_2 + 3H_2 \rightleftharpoons H_3C - OH + H_2O \quad (1)$$

$$\Delta H_{298} = 41.0\ \text{kJ mol}^{-1} \quad CO_2 + H_2 \rightleftharpoons CO + H_2O \quad (2)$$

Water concentrations in the range of 2−10 vol % specifically contribute to particle growth and a decrease of both the overall and Cu specific surface area due to its coordinating nature between nanosized particles.[17,29,33]

The use of promotors (e.g., Al_2O_3 or ZrO_2) contributes to catalytic activity and long-term stability, as they counteract the aggregation of particles at the nm scale and thus significantly increase Cu dispersion.[37−39] Thus, their impact on deactivation processes needs to be considered. For instance, the enrichment of $ZnAl_2O_4$ spinel out of crystalline ZnO and amorphous Al_2O_3 was described during the first 50 days of ToS in a CZA catalyst. This Zn−Al compound restrains the mentioned Cu−Zn interaction, hampering the active site. During this period, the domain sizes of ZnO and of the spinel significantly increase, while only a small rise in the domain size of Cu is observed. The deactivation in CZA materials was reported to proceed mainly by recrystallization of ZnO and the $ZnAl_2O_4$ spinel in the beginning (<50 days ToS).[30] Al_2O_3 as a promoter has a significant impact on Cu sintering being faster in comparison to conditions without additional water being present.[17] As mentioned before, zirconia is described as a promising promoter in terms of productivity and stability for CO_2-rich syngas feeds.[10−13,40] In comparison to CZA-based materials, the evolution of a ternary phase like $ZnAl_2O_4$ is not possible for Cu/ZnO/ZrO_2 (CZZ) materials.[30] However, the chemical states of Cu and Zn and their changes throughout catalyst operation in MeOH synthesis influenced by ZrO_2 as a catalyst dopant as well as the structural changes occurring on ZrO_2 itself are hardly described in the literature.

In the focus of the present study, catalysts from different stages of activation and the operating period are examined by different characterization techniques in order to determine the predominant structural changes and morphological transitions on the micro- and nanoscale. To assess a possible catalyst reactivation procedure, the reduction as well as rereduction is performed and the structural changes are analyzed.

EXPERIMENTAL SECTION

Continuous Coprecipitation. The CZZ precursor materials are prepared by continuous coprecipitation with subsequent aging. The details are described elsewhere.[41] In short, a solution of 117.42 g (0.49 mol) of copper(II)nitrate trihydrate ($Cu(NO_3)_2{\cdot}3H_2O$, Merck, Darmstadt, Germany, 99.5%), 72.29 g (0.24 mol) of zinc nitrate hexahydrate ($Zn(NO_3)_2{\cdot}6H_2O$, Alfa Aesar, Thermo Fisher, Kandel, Germany, 99%), and 27.48 (0.08 mol) of zirconium(IV)oxynitrate hexahydrate ($ZrO(NO_3)_2{\cdot}6H_2O$, Sigma-Aldrich/Merck, Darmstadt, Germany, 99%) in 3 L of deionized water is mixed under high volume flow to a solution of 1.01 mol L^{-1} $NaHCO_3$ at 55 °C. The suspension is transferred directly to a double-jacketed 5000 mL glass vessel and aged at 55 °C until the tipping point and 30 min beyond under stirring (1000 rpm). Following the aging period, the suspension is filtered, and the solid residue is washed with deionized water. The solid is then dried and calcined in air at 350 °C with a heating ramp of 3 K min^{-1} for 4 h, resulting in 30 g of a CZZ metal oxide precatalyst with a composition of 64/31/5 (Cu/Zn/Zr; mol %; normalized).

Catalyst Deactivation and Anoxic Sampling. The plant **Pa**rallel **C**atalyst **A**ging **S**etup (PaCAS) is used for systematic catalyst deactivation for methanol synthesis under lean synthesis gas mixtures (75 vol % N_2, 17 vol % H_2, 4 vol % CO, 4 vol % CO_2). The plant consists of two active reactors, enabling simultaneous deactivation of two different Cu-based catalysts. The catalysts are located in different blocks, which can be separated and displaced simply, thereby realizing variable sampling times of the catalysts. Therefore, the block can be easily disassembled and transferred into the glovebox for preparing samples for various analytical methods under an anoxic atmosphere.

For the reduction, the inlet pressure is set to 15 bar and the bed pressure is set to 2.5 bar. After this, a gas cylinder (5 vol % H_2 and 95 vol % N_2) is connected, and an equal flow rate for the different reactors can be adjusted by the flow indicators. The flow controller Defender 530 L 5−500 mL_N/min is mounted behind the pressure retention valve to measure the actual flow rate. The temperature program for the reduction is chosen as follows: 90 °C for 20 min and heating with a ramp of 10 K/min at 220 °C, then holding this temperature for 60 min. Then, the reactors are cooled to ambient temperature under an anoxic atmosphere. For the catalyst aging, a gas cylinder containing 17 vol % H_2, 4 vol % CO, 4 vol % CO_2, and 75 vol % N_2 is attached, and under an argon flow rate of 500 mL_N/min, the inlet pressure and the pressure retention valve are set to 70 and 60 bar, respectively. After heating to 260 °C, the gas dosing is changed to the synthesis gas feed, and during the aging program, the temperature, pressure, and flow rate are observed and readjusted, if necessary. During deactivation, the synthesis gas flow rate is kept at 120.7 mL_N/min to ensure proper aging conditions for the catalyst bed, according to the mass of the catalyst, and to ensure catalyst aging under thermodynamic control. To achieve a high dwell time, the catalyst mass-based volume flow is set to 5.00 L_N/g·h, which guarantees a long dwell time, leading to even aging of the catalyst. The flow rate ($\dot{V}_{2\text{reactors}}$) for both reactors is calculated as given in eq 3.

$$\dot{V}_{2r} = \frac{2\vartheta_{GHSV} m_{catalyst}}{60\,000} \quad (3)$$

After the reaction, the reactors are cooled to ambient temperature at an argon flow rate of 100 mL_N/min, and the catalyst bed is transferred into a glovebox (MBraun) by maintaining the materials in the reactor blocks under an argon atmosphere (99.9999% pure argon is used). All gases were used as received without additional drying of purification (99.999% N_2, 99.999% H_2, 99.995% CO_2, 99.97% CO).

X-ray Absorption Spectroscopic Experiments—Ex Situ and In Situ. The ex situ and in situ X-ray absorption spectroscopic (XAS) measurements were performed at the CATACT beamline[42] at the

KIT Light Source. For the ex situ measurements, 3 mg of the catalyst and 27 mg of dried hexagonal BN are mixed in the glovebox and filled into glass capillaries (Hilgenberg). Afterward, the capillaries are molten to keep the samples under an argon atmosphere to prevent oxidation. XAS data are recorded at the Cu K-edge (8.979 keV), Zn K-edge (9.659 keV), and Zr K-edge (17.998 keV). For the in situ measurements, the catalyst diluted with hexagonal BN (cat/BN = 1:9) is pressed and sieved (100−200 μm sieve fraction). Subsequently, ca. 100 mg of the mixture is deposited into a high-pressure transmission cell.[43,44]

The photon energy is selected by a Si(111) double-crystal monochromator and slightly detuned to suppress higher harmonics. The intensities of the incoming and transmitted monochromatic X-rays are measured with ionization chambers (Ohyo Koken Kogyo Co. Ltd., Japan, N_2 filling, 1 bar, 800 V) before and after the cell, as well as before and after a corresponding reference foil.[43]

The temperature-programmed reduction (TPR) is performed in a temperature range between 30 and 250 °C in a 5% H_2/N_2 flow (50 mL/min). For this purpose, three heating rates are used: 30 to 100 °C: 5 K/min, 100 to 150 °C: 2 K/min, and 150 to 250 °C: 1 K/min. During heating, Cu K-edge and Zn K-edge X-ray absorption near edge structure (XANES) data are each collected. Subsequently, the cell is cooled to 50 °C under a N_2 flow, and Cu K-edge and Zn K-edge extended X-ray absorption fine structure (EXAFS) data are recorded. Afterward, the cell is pressurized to 55 bar and heated to 260 °C at a defined feed gas flow (16.7% CO, 16.7% CO_2, 66.7% H_2, 50 mL/min) and kept for 3 h. Then, the cell is further heated to 290 °C at the same gas feed conditions and kept for another 3 h. Afterward, the cell is cooled to 50 °C under a N_2 flow, and EXAFS data at the Cu K-edge and Zn K-edge are recorded.

For the analysis of the XANES and EXAFS data, the Athena and Artemis-IFEFFIT/Demeter package (version 0.9.26)[45] is used. The data are calibrated using tabulated values for metallic reference foils ($E_{Cu,K}$ = 8979 eV; $E_{Zn,K}$ = 9659 eV; $E_{Zr,K}$ = 17998 eV). Afterward, the cubic spline background is subtracted to eliminate the nonstructural portion of absorption data, and the spectra are normalized.[46] For the refinement, k-ranges of 3−10 Å^{-1} for the Cu K-edge, 3.0−8.0 Å^{-1} for the Zn K-edge, and 3.0−8.0 Å^{-1} for the Zr K-edge are used. The amplitude factors (S_0^2) for Cu and Zn are set to 0.663 and 0.967, respectively (determined from the fitting of the experimental data on references; additional parameters in ESI: Table S3), and the coordination numbers for Cu in the first shell, second shell (Cu−"Cu"−Cu), and Zn−O−Zn shell were also evaluated.

X-ray Photoelectron Spectroscopy (XPS). For XPS analysis, the PHI 5000 VersaProbe II system (ULVAC-PHI Inc.) with a monochromatic Al Kα, $h\nu$ = 1486.7 eV, scanning microprobe X-ray source is used. Subsequently, the X-ray source power and the X-ray spot size diameter are adjusted to 30 W and 170 μm, respectively. By providing a pass energy of 187.85 eV of the analyzer, survey scans are recorded. Areas of the elemental lines were determined after Shirley background subtraction within an error of ±10−20%. Considering elemental sensitivity factors, asymmetry parameters, and the transmission function of the analyzer, the relative atomic concentrations are calculated. Narrow scans of the elemental lines are recorded at 23.5 eV pass energy, which yields an energy resolution of 0.69 eV fwhm at the Ag $3d_{5/2}$ elemental line of pure silver. In addition, calibration of the binding energy scale of the spectrometer is achieved via using well-established binding energies of elemental lines of pure metals (monochromatic Al Kα: Cu $2p_{3/2}$ at 932.62 eV, Au $4f_{7/2}$ at 83.96 eV).[47] The error of measured binding energies is estimated to be within ±0.2 eV.

For the XPS measurements, 5 mg of the catalyst is deposited on an indium foil inside a glovebox. Then, the sample is put in a transfer vessel and moved into the XPS analysis chamber under an anoxic atmosphere. The Fermi edges of the valence band prove that the samples are conductive and grounded. Furthermore, the measured binding energies of the elemental lines are compared to a reference database.[48,49] The ULVAC-PHI MultiPak program, version 9.9, was used for the data analysis.

Combustion Analysis for Determination of Light Elements (CHNS). CHNS analysis was used to investigate the poisoning of a catalyst and is carried out by weighing the sample in tin boats and heating them (1100 °C) in the presence of O_2, producing the product gases CO_2, H_2O, NO_2, and SO_2.[50,51] This is followed by controlled reduction of NO_2 to N_2 by passing the gas over Cu at 850 °C.[51] Finally, the product gas is captured by a column and identified using a thermal conductivity detector.[50] Here, a complete setup called vario EL cube from Elementar is used.

Inductive Coupled Plasma-Optical Emission Spectroscopy (ICP-OES). For the ICP-OES analysis of the CZZ catalyst, hydrofluoric acid digestion of 20 mg of the sample is carried out, enabling the determination of Cu, Zn, Zr, and poisons such as Fe or Ni (e.g., originating from metal tubes). Digestion is performed with an Anton Paar Multiwave 3000 microwave oven using HF (40%) in Teflon vessels at 240 °C for 2 h. Subsequent dilution is in 0.2 M HNO_3 Suprapur. For analysis, an Agilent 725 ICP-OES spectrometer with argon as plasma gas at 15 L/min and plasma stimulation at 40 MHz, 2 kW is used.

X-ray Diffraction (XRD). X-ray diffractograms were measured using a Panalytical X'Pert Pro X-ray diffractometer (Malvern Panalytical GmbH, Kassel, Germany) with Bragg−Brentano geometry and Cu Kα radiation with a Ni filter. The diffractograms are recorded in the range of 5−80° over a period of 120 min. The reflections are evaluated using HighScore Plus software (version 2.2.e (2.2.5)) and compared to references from the Joint Committee of Powder Diffraction Standards (JCPDS) database. To obtain the composition and particle size of the samples analyzed by XRD, Rietveld refinement is performed using the open-source program Profex 5.0.2 from Döbelin.[52]

N_2 Physisorption. N_2 physisorption measurements[53] were carried out on Quantachrome NOVA 2000e and NOVA 3200e devices (Anton Paar GmbH, Graz, Austria) at 77 K to determine pore size and active catalyst surface area. Samples (250 mg, grain size 250−500 μm) were degassed for 12 h at 230 °C. Isotherms are evaluated with the Brunnauer−Emmett−Teller (BET) model[54] in the range of 0.05−0.1 p/p0. The pore size distributions are calculated according to the Barret−Joyner−Halenda (BJH) method[55] using the desorption branch of the isotherm.

Infrared Spectroscopy (FTIR). Fourier transform infrared (FTIR) spectroscopy was performed with a Varian 660 FTIR spectrometer using the proprietary software Resolution Pro. The samples are ground with dried KBr (cat/KBr = 1:400) pressed for 15 min under 50 kN and measured in the range of 250−4000 cm^{-1} in transmission mode.

Scanning Electron Microscopy (SEM/EDXS). Field emission scanning electron microscopy (FESEM, Zeiss GeminiSEM 500 equipped with an energy-dispersive X-ray spectrometer EDXS, Oxford X-Max^N) was used to determine the morphology of the as-prepared CZZ materials and for semiquantitative elemental analysis. For this, 2 mg of the powder material is deposited onto a sample holder by a gluey carbon film.

Transmission Electron Microscopy (TEM/EDXS). High-angle annular dark-field scanning transmission electron microscopy (HAADF-STEM) imaging combined with energy-dispersive X-ray spectroscopy (EDXS) was used for semiquantitative analysis of the chemical composition and the metal dispersion on the nanometer scale. For characterization, an FEI Osiris ChemiSTEM microscope operated at 200 keV, equipped with a Bruker Quantax system (XFlash detector) for EDXS measurements, was used. TEM sample preparation is performed by mixing the CZZ powders with ultrapure water and dispensing one droplet of the suspension onto a lacey carbon film TEM grid using an ultrasonic nebulizer. To obtain mean particle sizes, the size of more than 200 particles has been determined from several HAADF-STEM images (with ImageJ 1.47v software). From the measured length, the mean size and standard deviation are calculated as classical statistical descriptors.[56]

RESULTS AND DISCUSSION

Anoxic Handling as a Prerequisite Leading to a Specific Setup. For reduced and operating methanol synthesis catalysts being sensitive to oxygen (e.g., due to oxidation of Cu^0/Cu^0Zn^0 species), a new setup has been designed and constructed. Its main purpose is to enable parallel catalyst deactivation under static conditions and ensure anoxic withdrawal (**Pa**rallel **C**atalyst **A**ging **S**etup = PaCAS; see details in the Experimental Section above). With this setup, oxidation of the catalyst material can be excluded within the respective methodological error ranges (ESI: Figure S1).

Activity Decrease. Examined catalyst samples are denominated as calcined (denoted CZZ_{calc} or −50 h ToS), reduced (CZZ_{red}), and aged (CZZ_{50h}, CZZ_{935h} ToS). The catalyst's performance shows a loss in methanol concentration of approximately 13% for CZZ_{935h} in comparison to freshly prepared CZZ_{red} (Figure 1). This is in the range of literature-

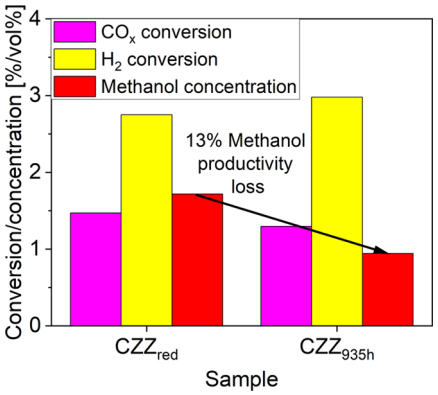

Figure 1. Conversion of CO_x, H_2, and methanol concentration in product gas. Product gas concentration for all species is shown in ESI: Figure S2. Conditions: 260 °C, 60 bar, H_2/CO_x = 2.13, CO_2/CO_x = 0.5, GHSV = 3300 h^{-1}.

known performance decreases considering the specific conditions employed here (see experimental section).[29] Sintering of the active species (e.g., Cu and ZnO) is only assumed to be the driver for the described activity loss at this point.

Surface Phenomena and Composition Considerations. STEM measurements indicate (Figure 2, green) that the mean particle size of CZZ does not change significantly before

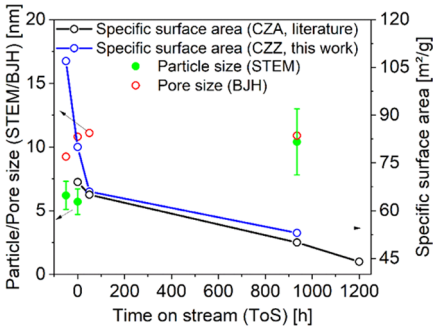

Figure 2. Specific surface area determined by N_2 physisorption (blue circles), mean pore size (red circles), and mean particle size (green filled circles) for CZZ_{calc}, CZZ_{red}, CZZ_{50h}, and CZZ_{935h} with observed values from the literature (black circles; CZA). Data reproduced with permission from ref 30. Copyright 2016 Wiley-VCH.

($CZZ_{calc.}$: 6.2 ± 1.1 nm) and after reduction ($CZZ_{red.}$: 5.7 ± 1.0 nm). However, for CZZ_{935h}, a significant increase (10.4 ± 2.6 nm) results. On the other hand, the mean pore size (assessed by the BJH plot) increases and the specific surface area declines already after reduction (Figure 2, red and blue). The pore size remains widely constant (11 nm) during subsequent catalyst aging, but the specific surface area decreases slightly further in narrow accordance with the literature (Figure 2, black).[30] For example, CZZ_{red} shows a specific surface area of 80 m^2/g ($CZA_{Literature, red}$ = 69 m^2/g), which declines to 53 m^2/g for CZZ_{935h} ($CZA_{Literature, 935h}$ = 50 m^2/g). A first assumption for this behavior is that small pores are blocked during the reduction (pore volumes are 0.336 mL/g before reduction and 0.281 mL/g afterward, in addition to the increase of mean pore size) due to the presence of so-called "high-temperature carbonate," which is known to be present in Cu/ZnO (CZ)-type catalysts after calcination in the form of $M_2O_{1.5}(CO_3)_{0.5}$,[57] where M represents the sum of both Cu and Zn. Under reducing conditions, the pore-stabilizing carbonate will decompose, thus leading to pore blocking. However, CHNS analysis and XPS measurements do not show significant changes for carbon species (see also ESI: Table S2 and the respective text section). Thus, we are not able to confirm carbonate species to be an explanation for pore blockage and conclude that the temperature-induced mobility of Cu^0 and the large capillary forces in small pores predominantly contribute to this phenomenon.

Before reduction, Cu and Zn in CZZ_{calc} exist in their oxidic form with primary particle sizes below the 100 nm scale (proven by a combination of SEM/TEM/EDXS (ESI: Figures S4 and S5) and XRD (ESI: Figure S3)), whereas the small amount of ZrO_2 (approximately 5 wt %) remains undetectable by XRD.

X-ray photoelectron spectroscopy has been performed to investigate the surface changes on the CZZ material. After reduction, Cu was found in its elemental state even after 935 h ToS (compare also ESI: Figure S1). During reduction, ZnO_x enriches on the catalyst's surface, while copper impoverishes (seen as changes in the corresponding peak intensities in XPS spectra, Figure 3), in line with the proposed formation of a ZnO_x overlayer, confirmed by TEM measurements.[30,36] Lunkenbein et al. found that ZnO crystallizes throughout catalysis, leading to a rigid and nonflexible overlayer.[30,36] The authors proved that this overlayer was formed immediately after reduction.

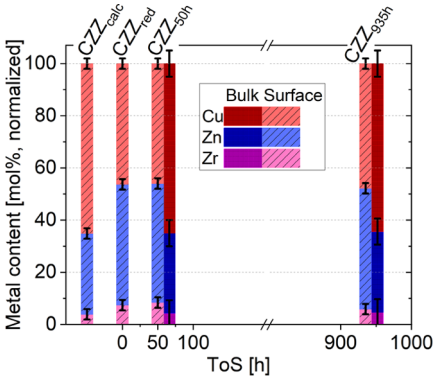

Figure 3. Composition of the catalyst determined by XPS (surface sensitive, pale colors, and stripes) and ICP-OES (bulk composition, dark colors) after defined ToS.

Structural and Coordination Changes. XAS measurements (Figure 4) at the Cu K- ad Zn K-edges and data from

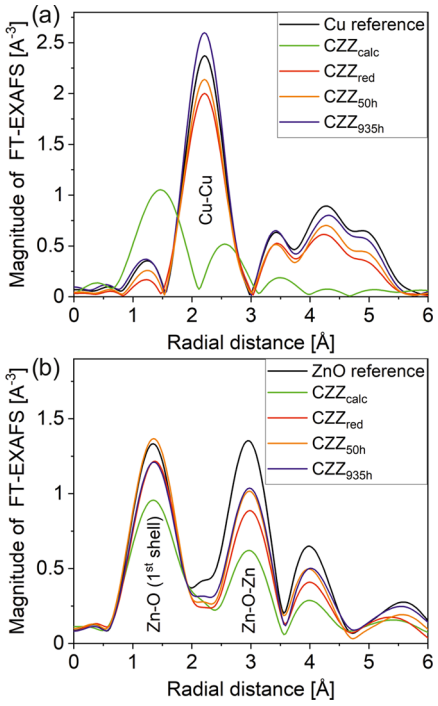

Figure 4. Magnitude of k^2-weighted FT-EXAFS data of the calcined (green), reduced (red), and aged (orange and blue) CZZ catalysts at (a) the Cu K-edge and (b) Zn K-edge (not phase-corrected).

the respective EXAFS show some less significant increase of Cu and ZnO particle size throughout aging, derived from peak intensities corresponding to the Cu−Cu(−Cu) first and second coordination shells as well as the Zn−O−Zn coordination (Table 1).

Table 1. Coordination Numbers (CN) of Cu and Zn Coordination Shells at Different ToS (Details are in ESI: Table S3)

sample state	CN (Cu−Cu)	CN (Cu−Cu−Cu)	CN (Zn−O−Zn)
CZZ$_{calc}$	N/A	N/A	3.1 ± 1.7
CZZ$_{red}$	10.1 ± 1.7	3.7 ± 1.6	5.1 ± 2.1
CZZ$_{50h}$	11.9 ± 1.8	4.1 ± 1.6	5.5 ± 2.4
CZZ$_{935h}$	12.7 ± 2.0	5.2 ± 1.9	5.7 ± 2.3

The particle size can be estimated from the signal height according to CNs of the corresponding coordination shells individually for every element, but the dependence is nonlinear and saturates fast for sizes above 5 nm, which is an estimated upper (size) detection limit for this method.[58,59] As mentioned above, the overall particle size increases from CZZ$_{red}$ to CZZ$_{935h}$ (compare Figure 2), in agreement with the observations from Cu K EXAFS data.

In contrast to CZA materials, where ZnO crystallizes by forming $ZnAl_2O_4$, before Cu sintering is enhanced,[30] ZnO and Cu^0 sinter/crystallize simultaneously within the CZZ studied here. Prior to reduction, a mixture of metal oxides on the sub-100 nm scale is observed (see ESI: Figures S3−S5). A small contribution of the postedge structure of EXAFS at the Cu K-edge overlaps with the Zn K XANES and might additionally lead to deviations in the spectrum (ESI: Figure S11), causing some uncertainty in data interpretation. The peak in the FT-EXAFS data of the Zn K-edge corresponds to the first coordination shell (Zn−O) and changes for the samples at different ToS, which might hint at the structural refinement of ZnO_x coordination during the reduction and reaction (Figure 4b). The analysis of the evolution of the second coordination shell of ZnO (Zn−O−Zn) allows us to indirectly estimate the sintering strength of ZnO species, as the formation of the long-range ordered structure indicates the growing of ZnO particles with a stable coordination structure of [ZnO_4] tetrahedra. In the mixed metal oxide (CZZ$_{calc.}$), ZnO contributes less to Zn−O−Zn scattering at the Zn K-edge than in nanocrystalline ZnO (e.g., a ZnO_x overlayer). The CN of the Zn−O−Zn coordination shell significantly increases after reduction (CZZ$_{red}$) compared to CZZ$_{calc}$, which indicates restructuring of Zn−O−Zn and might hint at ZnO_x overlayer formation accompanied by crystallization of already present ZnO nanoparticles. For CZZ$_{50h}$ and CZZ$_{935h}$, ZnO undergoes further sintering/crystallizing, resulting in smaller particle sizes compared to Cu, below the respective saturation limit (approximately 5 nm). Due to the similarity of scattering profiles for Cu and Zn, nanostructured ZnO and mixed $CuZnO_x$ particles are not reliably distinguishable by EXAFS.

Role of the Zirconia Promoter. The low zirconia content in the CZZ catalyst studied here (approximately 5 wt % Zr) hampers it from obtaining reliable data by operando XAS or ex situ XRD measurements. On the other hand, we were able to achieve ex situ FT-EXAFS data at the Zr K-edge, which confirms the monoclinic structure of zirconia after calcination remaining after reduction and also after aging (Figure 5a).

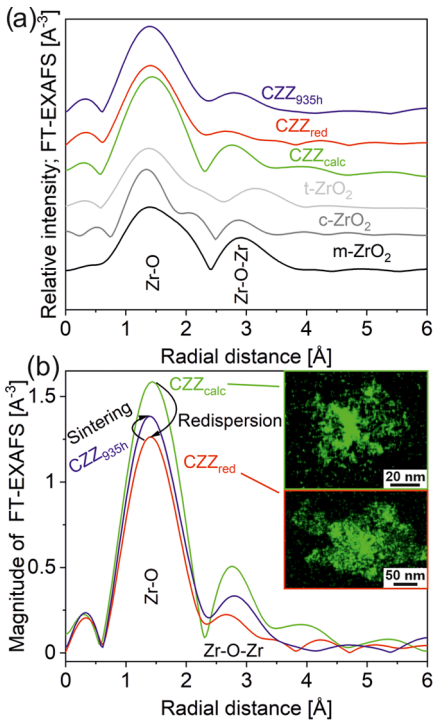

Figure 5. Magnitude of the Zr K FT-EXAFS data (not phase-corrected) of the calcined (green), reduced (red), and aged (blue) CZZ catalysts as well as the TEM/EDXS maps for Zr in the calcined and reduced states as insets. (a) Stacked plot with references for tetragonal, cubic, and monoclinic ZrO_2. (b) Overlaying plot.

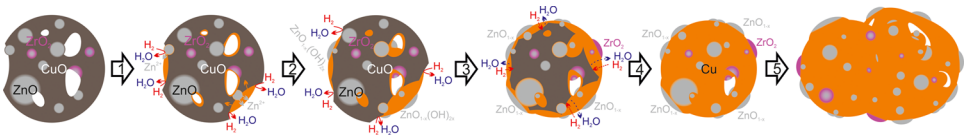

Figure 6. Mechanism of reduction and aging of a CZZ system: the reduction of a mixed metal oxide constituted of CuO (dark brown), ZnO (gray), and ZrO_2 (magenta) followed by reduction of small seeds of Cu^0 (orange) and forming a ZnO_x overlayer with redispersion of ZrO_2, Cu^0 particle shrinking, and blocking of small pores as well as overlayer growth and sintering.

Changes of Zr−O and Zr−O−Zr coordination shells hint at a possible redispersion of zirconia particles upon reduction (Figure 5b) underlined by TEM/EDXS measurements (Figure 5b inset; ESI: Figure S5h−p). Accounting for the increase in particle size indicated by FT-EXAFS for Cu and Zn with no overall increase in overall particle size (by STEM, see Figure 2) reinforces the aforementioned assumption of zirconia redispersion. Therefore, we assume that zirconia redispersion upon reduction could be attributed to the formation of hydroxide species and reorganization of the overall particle orientation. The reducing conditions produce water, which itself may hydrate ZrO_2. Despite the reducing conditions, oxygen vacancy formation can be excluded at this point (by XPS data). After catalyst operation, however, the average particle size of ZrO_2 (TEM/EDXS) is again higher after 935 h ToS as well as Zr−O and Zr−O−Zr coordination increases. Taken together, the role of ZrO_2 as important promoting but not fully inert material remains as its nanostructure changes during reduction/operation.

Overall Changes on the Nanoscale over Time. Based on the data discussed in the previous sections and according to mechanisms discussed in the literature, a possible scheme for changes in the nanostructure during reduction and aging is proposed (Figure 6). Upon reduction, small seeds of Cu^0 in the metal oxide mixture initially emerge (Step 1). These seeds then grow autocatalytically,[27,60] accompanied by the enrichment of both Zn^{2+} and Zr^{4+} on the particle surface due to their immiscibility with Cu^0 and their larger resistance against reduction at these conditions (5 vol % H_2/N_2; Step 2). As water is produced during the reduction of CuO, a $ZnO_{1-x}(OH)_{2x}$ layer forms on the Cu^0 particle surface, increasing the stacking fault probability.[31] In parallel, a small amount of zirconia from inside the mixture is deposited on the surface, causing its redispersion. Further reduction of the particle core is then delayed due to diffusion limitation (Step 3).[61] At least, a mixed $Cu^0/ZnO_x/ZrO_2$ particle is present (Step 4), which is smaller in size due to the plunging of the smaller pores within (Steps 2−4, also see page 16). Cu^0 exhibits higher mobility here (220 °C, Hüttig temperature of 134 °C),[33,34] and the particle size then increases throughout reduction and even more during aging, as the Cu^0/ZnO_x particles as well as the ZnO_x overlayer grow and crystallization proceeds (Step 5). In summary, irreversible structural changes are attributed mainly to the segregation of Cu, ZnO_x, and ZrO_2, hampering the catalyst's activity. The activity loss described in Figure 1 can be tentatively attributed to the loss of active surface area (compare Figure 2) and sintering of Cu^0, as analogously proposed for CZA systems.[30]

Consequences for Possible Catalyst Regeneration. To investigate the progress of a potential regeneration, in situ XANES data were measured at reduction conditions (5 vol % H_2/N_2, 50−250 °C) and compared for CZZ_{calc} and air-exposed CZZ_{935h}. ESI: Figure S7 shows the results of a linear combination analysis (LCA) of Cu K XANES data during the reduction with Cu and CuO as regarded components. It is observed that reduction largely takes place at around 160 °C for both catalyst materials. In the case of air-exposed CZZ_{935h}, reduction starts at a lower temperature (100 °C) and ends at a higher temperature (190 °C) compared to CZZ_{calc} (range of 130−180 °C, also reflected in the first derivative shown in the respective figure). Cu is completely reduced in both CZZ_{calc} and air-exposed CZZ_{935h} at the end of the reduction period. It seems likely that the broader particle size distribution of CZZ_{935h} with average larger particles is responsible for the observed temperature-dependent course, since smaller nanoparticles are usually more reactive in the reduction, whereas larger particles need higher activation energy for full reduction. The structural changes occurring due to the aging of the catalysts are not collaterally reversible by subsequent reduction.

Cu K EXAFS data on air-exposed CZZ_{935h} differ from the data of the CuO reference but hint at the partial oxidation of Cu and the presence of a mixed Cu^0/CuO/ZnO state in this sample (Figure 7a and ESI: Figure S10). Additionally, the

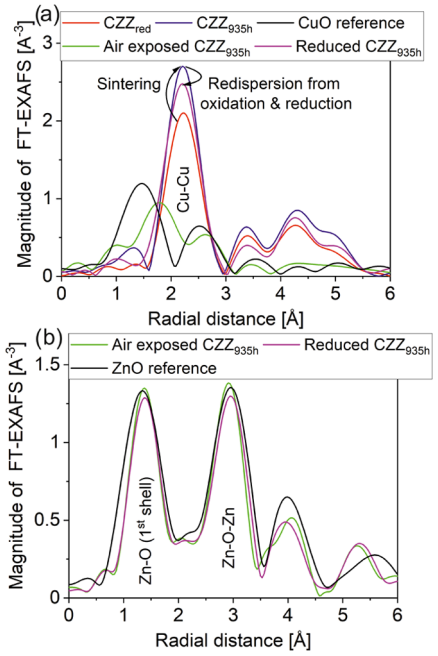

Figure 7. FT-EXAFS of the in situ reduced catalyst sample (magenta) at the Cu K-edge (a) and Zn K-edge (b) for CZZ_{935h} (blue), which has been exposed to air before (green).

decrease of the peak intensity of the Cu−Cu coordination shell indicates a redispersion of Cu particles after rereduction (Figure 7a, transition from blue to red). Considering the intensity of the peak corresponding to the second coordination sphere of the Zn K FT-EXAFS, no sintering or redispersion of the ZnO particles takes place at the air-exposed and

subsequently in situ reduced CZZ_{935h} (Figure 7b). This is in contrast to initial reduction of the freshly calcined CZZ described in the prior chapter, where ZnO sinters significantly already during reduction.

CONCLUSIONS

An experimental setup was developed and constructed to study materials with respect to catalyst deactivation in methanol synthesis, ensuring complete anoxic conditions upon catalyst withdrawal and characterization. Structural and morphological changes of a CZZ catalyst at different stages up to 935 h ToS in methanol synthesis were investigated and compared by different methods. In catalysis experiments, a high-purity syngas mixture was used, for which no indications of catalyst deactivation by coking and poisoning were found at the conditions considered here.

Significant changes, however, are a decrease in the specific surface area and an expansion of either particle size or crystallinity. These subprocesses already start during reduction, accompanied by an accumulation of ZnO_x at the catalyst surface. Interestingly, the average particle size remains similar before and after reduction, while only the average pore size increases. We hypothesize that starting from a microstructural mixture of CuO, ZnO, and ZrO_2, a ZnO_x overlayer is formed on the reduced Cu^0 particles during reduction, analogous to model ideas proposed for CZA catalysts in the literature. Initially, the structural influence of ZrO_2 appears to be essentially mechanically stabilizing, similar to Al_2O_3 in CZA catalysts. On the other hand, there are clear indications of structural changes as a result of redispersion, which leads to measurable particle growth in the course of prolonged use in methanol synthesis. Regeneration of the material structure by means of reduction of the aged and air-exposed catalyst succeeds only incompletely due to the demixing of Cu and Zn species, as was demonstrated by means of XAS measurements.

Based on these findings, we will subsequently address the influence of model components for possible impurities in the synthesis gas. This concerns both the use of CO_2-rich syngas and possible minor components in hydrogen that is electrolytically produced and purified in a different way than conventionally produced hydrogen from natural gas.

AUTHOR INFORMATION

Corresponding Author

Lucas Warmuth − *Institute of Catalysis Research and Technology (IKFT), Karlsruhe Institute of Technology (KIT), 76344 Eggenstein-Leopoldshafen, Germany;* orcid.org/0000-0002-2234-028X; Email: lucas.warmuth3@kit.edu

Authors

Matthias Steurer − *Institute of Catalysis Research and Technology (IKFT), Karlsruhe Institute of Technology (KIT), 76344 Eggenstein-Leopoldshafen, Germany;* Present Address: Institute for Applied Physics (APH), Karlsruhe Institute of Technology (KIT), 76131 Karlsruhe, Germany

Dieter Schild − *Institute for Nuclear Waste Disposal (INE), Karlsruhe Institute of Technology (KIT), 76344 Eggenstein-Leopoldshafen, Germany;* orcid.org/0000-0001-6034-8146

Anna Zimina − *Institute of Catalysis Research and Technology (IKFT), Karlsruhe Institute of Technology (KIT), 76344 Eggenstein-Leopoldshafen, Germany; Institute for Chemical Technology and Polymer Chemistry (ITCP), Karlsruhe Institute of Technology (KIT), 76131 Karlsruhe, Germany;* orcid.org/0000-0002-3111-7741

Jan-Dierk Grunwaldt − *Institute of Catalysis Research and Technology (IKFT), Karlsruhe Institute of Technology (KIT), 76344 Eggenstein-Leopoldshafen, Germany; Institute for Chemical Technology and Polymer Chemistry (ITCP), Karlsruhe Institute of Technology (KIT), 76131 Karlsruhe, Germany;* orcid.org/0000-0003-3606-0956

Stephan Pitter − *Institute of Catalysis Research and Technology (IKFT), Karlsruhe Institute of Technology (KIT), 76344 Eggenstein-Leopoldshafen, Germany*

Author Contributions

$^{\perp}$L.W. and M.S. contributed equally to this work. The manuscript was written through contributions of all authors. All authors have given approval to the final version of the manuscript. L.W. and M.S. did work with the setup and prepared samples for analysis. Furthermore, L.W. wrote the manuscript. D.S., L.W., M.S., and A.Z. performed measurements and data analyses. Moreover, M.S., D.S., A.Z., J.-D.G., and S.P. contributed to scientific discussions and interpretations and revised the manuscript.

Funding

The authors are grateful to the Helmholtz Innovation Pool "Solar Hydrogen," a project within the Helmholtz Program Materials and Technologies for the Energy Transition (MTET), project no. 38.04.03.

Notes

The authors declare no competing financial interest.

ACKNOWLEDGMENTS

The authors would like to thank the Institute for Beam Physics and Technology (IBPT) for the operation of the storage ring, the Karlsruhe Research Accelerator (KARA). The authors acknowledge the KIT Light Source for the provision of instruments at the CATACT beamline of the Institute of Catalysis Research and Technology (IKFT), Institute for Nuclear Waste Disposal (INE), and Institute for Chemical Technology and Polymer Chemistry (ITCP). Furthermore, the authors thank Danielle Santos Goncalves, Diana Deutsch, Moritz Herfet, and Gabriela Rodrigues Niquini (IKFT) for their help and technical support during experiments. Additionally, the authors thank Lorena Baumgarten, Mariam Schulte, Dimitry Doronkin, and Alexey Boubnov for their help in introducing, plotting, and fitting EXAFS spectra. Moreover, the authors are grateful to the whole IKFT analytics and the people providing them, especially Thomas Zevaco, Thomas Otto, Michael Zimmermann, and Armin Lautenbach. Finally, the authors thank the laboratory for electron

microscopy (LEM) at KIT and especially Radian Popescu and Heike Störmer for TEM measurements.

DEDICATION

This work is dedicated to Prof. Dr. Eckhard Dinjus on the occasion of his 80th birthday.

ABBREVIATIONS

BET, Brunnauer–Emmett–Teller; BJH, Barret–Joyner–Halenda; CN, coordination number; CZA, $Cu/ZnO/Al_2O_3$; CZZ, $Cu/ZnO/ZrO_2$; EDXS, energy-dispersive X-ray spectroscopy; EXAFS, extended X-ray absorption fine structure; FTIR, Fourier transform infrared; GHSV, gas hourly space velocity; HAADF-STEM, high-angle annular dark-field scanning transmission electron microscopy; ICP-OES, inductive coupled plasma-optical emission spectroscopy; LCA, linear combination analysis; PaCAS, parallel catalyst aging setup; TEM, transmission electron microscopy; SEM, scanning electron microscopy; SMSI, strong metal support interaction; TPR, temperature-programmed reduction; XANES, X-ray absorption near edge structure; XAS, X-ray absorption spectroscopy; XRD, X-ray diffraction; XPS, X-ray photoelectron spectroscopy

REFERENCES

(1) Navarro-Jaén, S.; Virginie, M.; Bonin, J.; Robert, M.; Wojcieszak, R.; Khodakov, A. Y. Highlights and Challenges in the Selective Reduction of Carbon Dioxide to Methanol. *Nat. Rev. Chem.* **2021**, *5* (8), 564–579.

(2) Sehested, J. Industrial and Scientific Directions of Methanol Catalyst Development. *J. Catal.* **2019**, *371*, 368–375.

(3) Bertau, M.; Schmidt, F.; Wernicke, H.-J.; Offermanns, H.; Plass, L. *Methanol: The Basic Chemical and Energy Feedstock of the Future:Asinger's Vision Today*; Springer, 2014.

(4) The Methanol Industry, 2011. https://www.methanol.org/the-methanol-industry/ (accessed October 11, 2023).

(5) Suseno, T.; Umar, D. F. Prospect of Coal-Based Methanol Market in Indonesia. *IOP Conf. Ser.: Earth Environ. Sci.* **2021**, *882* (1), No. 012073.

(6) Fujita, S.-i.; Satriyo, A. M.; Shen, G. C.; Takezawa, N. Mechanism of the Formation of Precursors for the Cu/ZnO Methanol Synthesis Catalysts by a Coprecipitation Method. *Catal. Lett.* **1995**, *34* (1–2), 85–92.

(7) Bems, B.; Schur, M.; Dassenoy, A.; Junkes, H.; Herein, D.; Schlögl, R. Relations between Synthesis and Microstructural Properties of Copper/Zinc Hydroxycarbonates. *Chem. - Eur. J.* **2003**, *9* (9), 2039–2052.

(8) Behrens, M.; Girgsdies, F.; Trunschke, A.; Schlögl, R. Minerals as Model Compounds for Cu/ZnO Catalyst Precursors: Structural and Thermal Properties and IR Spectra of Mineral and Synthetic (Zincian) Malachite, Rosasite and Aurichalcite and a Catalyst Precursor Mixture. *Eur. J. Inorg. Chem.* **2009**, *2009* (10), 1347–1357.

(9) Kalz, K. F.; Kraehnert, R.; Dvoyashkin, M.; Dittmeyer, R.; Gläser, R.; Krewer, U.; Reuter, K.; Grunwaldt, J.-D. Future Challenges in Heterogeneous Catalysis: Understanding Catalysts under Dynamic Reaction Conditions. *ChemCatChem* **2017**, *9* (1), 17–29.

(10) Wild, S.; Polierer, S.; Zevaco, T. A.; Guse, D.; Kind, M.; Pitter, S.; Herrera Delgado, K.; Sauer, J. Direct DME Synthesis on CZZ/H-FER from variable CO_2/CO Syngas Feeds. *RSC Adv.* **2021**, *11* (5), 2556–2564.

(11) Lam, E.; Larmier, K.; Wolf, P.; Tada, S.; Safonova, O. V.; Copéret, C. Isolated Zr Surface Sites on Silica Promote Hydrogenation of CO_2 to CH_3OH in Supported Cu Catalysts. *J. Am. Chem. Soc.* **2018**, *140* (33), 10530–10535.

(12) Tada, S.; Katagiri, A.; Kiyota, K.; Honma, T.; Kamei, H.; Nariyuki, A.; Uchida, S.; Satokawa, S. Cu Species Incorporated into Amorphous ZrO_2 with High Activity and Selectivity in CO_2-to-Methanol Hydrogenation. *J. Phys. Chem. C* **2018**, *122* (10), 5430–5442.

(13) Behrens, M.; Schlögl, R. How to Prepare a Good Cu/ZnO Catalyst or the Role of Solid State Chemistry for the Synthesis of Nanostructured Catalysts. *Z. Anorg. Allg. Chem.* **2013**, *639* (15), 2683–2695.

(14) Arena, F.; Italiano, G.; Barbera, K.; Bordiga, S.; Bonura, G.; Spadaro, L.; Frusteri, F. Solid-State Interactions, Adsorption Sites and Functionality of Cu-ZnO/ZrO_2 Catalysts in the CO_2 Hydrogenation to CH_3OH. *Appl. Catal., A* **2008**, *350* (1), 16–23.

(15) Larmier, K.; Liao, W.-C.; Tada, S.; Lam, E.; Verel, R.; Bansode, A.; Urakawa, A.; Comas-Vives, A.; Copéret, C. CO_2-to-Methanol Hydrogenation on Zirconia-Supported Copper Nanoparticles: Reaction Intermediates and the Role of the Metal-Support Interface. *Angew. Chem., Int. Ed.* **2017**, *56* (9), 2318–2323.

(16) Polierer, S.; Jelic, J.; Pitter, S.; Studt, F. On the Reactivity of the Cu/ZrO_2 System for the Hydrogenation of CO_2 to Methanol: A Density Functional Theory Study. *J. Phys. Chem. C* **2019**, *123* (44), 26904–26911.

(17) Prašnikar, A.; Pavlišič, A.; Ruiz-Zepeda, F.; Kovač, J.; Likozar, B. Mechanisms of Copper-Based Catalyst Deactivation during CO_2 Reduction to Methanol. *Ind. Eng. Chem. Res.* **2019**, *58* (29), 13021–13029.

(18) Wu, J.; Saito, M.; Takeuchi, M.; Watanabe, T. The Stability of Cu/ZnO-based Catalysts in Methanol Synthesis from a CO_2-Rich Feed and from a CO-Rich Feed. *Appl. Catal., A* **2001**, *218* (1–2), 235–240.

(19) Twigg, M. V. Deactivation of Copper Metal Catalysts for Methanol Decomposition, Methanol Steam Reforming and Methanol Synthesis. *Top. Catal.* **2003**, *22* (3/4), 191–203.

(20) Moulijn, J.; van Diepen, A.; Kapteijn, F. Catalyst Deactivation: Is It Predictable? *Appl. Catal., A* **2001**, *212* (1–2), 3–16.

(21) Sobczak, J.; Wysocka, I.; Murgrabia, S.; Rogala, A. A Review on Deactivation and Regeneration of Catalysts for Dimethyl Ether Synthesis. *Energies* **2022**, *15* (15), No. 5420.

(22) Laudenschleger, D.; Ruland, H.; Muhler, M. Identifying the Nature of the Active Sites in Methanol Synthesis over Cu/ZnO/Al_2O_3 Catalysts. *Nat. Commun.* **2020**, *11* (1), No. 3898.

(23) Hansen, J. B.; Nielsen, P. E. H. Methanol Synthesis. In *Handbook of Heterogeneous Catalysis*; John Wiley & Sons, 2008; pp 2920–2949.

(24) Sun, J. T.; Metcalfe, I. S.; Sahibzada, M. Deactivation of Cu/ZnO/Al_2O_3 Methanol Synthesis Catalyst by Sintering. *Ind. Eng. Chem. Res.* **1999**, *38* (10), 3868–3872.

(25) Grunwaldt, J.-D.; Molenbroek, A.; Topsøe, N.-Y.; Topsøe, H.; Clausen, B. In Situ Investigations of Structural Changes in Cu/ZnO Catalysts. *J. Catal.* **2000**, *194* (2), 452–460.

(26) Pandit, L.; Boubnov, A.; Behrendt, G.; Mockenhaupt, B.; Chowdhury, C.; Jelic, J.; Hansen, A.-L.; Saraçi, E.; Ras, E.-J.; Behrens, M.; Studt, F.; Grunwaldt, J.-D. Unravelling the Zn-Cu Interaction during Activation of a Zn-Promoted Cu/MgO Model Methanol Catalyst. *ChemCatChem.* **2021**, *13* (19), 4120–4132.

(27) Beck, A.; Zabilskiy, M.; Newton, M. A.; Safonova, O.; Willinger, M. G.; van Bokhoven, J. A. Following the Structure of Copper-Zinc-Alumina across the Pressure Gap in Carbon Dioxide Hydrogenation. *Nat. Catal.* **2021**, *4* (6), 488–497.

(28) Liang, B.; Ma, J.; Su, X.; Yang, C.; Duan, H.; Zhou, H.; Deng, S.; Li, L.; Huang, Y. Investigation on Deactivation of Cu/ZnO/Al_2O_3 Catalyst for CO_2 Hydrogenation to Methanol. *Ind. Eng. Chem. Res.* **2019**, *58* (21), 9030–9037.

(29) Fichtl, M. B.; Schlereth, D.; Jacobsen, N.; Kasatkin, I.; Schumann, J.; Behrens, M.; Schlögl, R.; Hinrichsen, O. Kinetics of Deactivation on Cu/ZnO/Al_2O_3 Methanol Synthesis Catalysts. *Appl. Catal., A* **2015**, *502*, 262–270.

(30) Lunkenbein, T.; Girgsdies, F.; Kandemir, T.; Thomas, N.; Behrens, M.; Schlögl, R.; Frei, E. Bridging the Time Gap: A Copper/Zinc Oxide/Aluminum Oxide Catalyst for Methanol Synthesis

Studied under Industrially Relevant Conditions and Time Scales. *Angew. Chem., Int. Ed.* **2016**, *55* (41), 12708−12712.
(31) Behrens, M.; Studt, F.; Kasatkin, I.; Kühl, S.; Hävecker, M.; Abild-Pedersen, F.; Zander, S.; Girgsdies, F.; Kurr, P.; Kniep, B.-L.; Tovar, M.; Fischer, R. W.; Nørskov, J. K.; Schlögl, R. The Active Site of Methanol Synthesis over $Cu/ZnO/Al_2O_3$ Industrial Catalysts. *Science* **2012**, *336* (6083), 893−897.
(32) Frei, E.; Gaur, A.; Lichtenberg, H.; Zwiener, L.; Scherzer, M.; Girgsdies, F.; Lunkenbein, T.; Schlögl, R. Cu−Zn Alloy Formation as Unfavored State for Efficient Methanol Catalysts. *ChemCatChem* **2020**, *12* (16), 4029−4033.
(33) Bozzano, G.; Manenti, F. Efficient Methanol Synthesis: Perspectives, Technologies and Optimization Strategies. *Prog. Energy Combust. Sci.* **2016**, *56*, 71−105.
(34) Tohji, K.; Udagawa, Y.; Mizushima, T.; Ueno, A. The Structure of the Copper/Zinc Oxide Catalyst by an in-situ EXAFS Study. *J. Phys. Chem. A* **1985**, *89* (26), 5671−5676.
(35) Goesmann, H.; Feldmann, C. Nanopartikuläre Funktionsmaterialien. *Angew. Chem.* **2010**, *122* (8), 1402−1437.
(36) Lunkenbein, T.; Schumann, J.; Behrens, M.; Schlögl, R.; Willinger, M. G. Formation of a ZnO Overlayer in Industrial $Cu/ZnO/Al_2O_3$ Catalysts induced by strong Metal-Support Interactions. *Angew. Chem., Int. Ed.* **2015**, *54* (15), 4544−4548.
(37) Prieto, G.; Zečević, J.; Friedrich, H.; de Jong, K. P.; de Jongh, P. E. Towards Stable Catalysts by Controlling Collective Properties of Supported Metal Nanoparticles. *Nat. Mater.* **2013**, *12* (1), 34−39.
(38) Sánchez-Contador, M.; Ateka, A.; Rodriguez-Vega, P.; Bilbao, J.; Aguayo, A. T. Optimization of the Zr Content in the CuO-ZnO-ZrO_2 /SAPO-11 Catalyst for the Selective Hydrogenation of CO +CO_2 Mixtures in the Direct Synthesis of Dimethyl Ether. *Ind. Eng. Chem. Res.* **2018**, *57* (4), 1169−1178.
(39) Arena, F.; Mezzatesta, G.; Zafarana, G.; Trunfio, G.; Frusteri, F.; Spadaro, L. Effects of Oxide Carriers on Surface Functionality and Process Performance of the Cu−ZnO System in the Synthesis of Methanol via CO_2 Hydrogenation. *J. Catal.* **2013**, *300*, 141−151.
(40) Wang, W.; Qu, Z.; Song, L.; Fu, Q. CO_2 hydrogenation to methanol over Cu/CeO_2 and Cu/ZrO_2 catalysts: Tuning methanol selectivity via metal-support interaction. *J. Energy Chem.* **2020**, *40*, 22−30.
(41) Polierer, S.; Guse, D.; Wild, S.; Delgado, K. H.; Otto, T. N.; Zevaco, T. A.; Kind, M.; Sauer, J.; Studt, F.; Pitter, S. Enhanced Direct Dimethyl Ether Synthesis from CO_2-Rich Syngas with $Cu/ZnO/ZrO_2$ Catalysts Prepared by Continuous Co-Precipitation. *Catalysts* **2020**, *10* (8), No. 816.
(42) Zimina, A.; Dardenne, K.; Denecke, M. A.; Doronkin, D. E.; Huttel, E.; Lichtenberg, H.; Mangold, S.; Pruessmann, T.; Rothe, J.; Spangenberg, T.; Steininger, R.; Vitova, T.; Geckeis, H.; Grunwaldt, J.-D. CAT-ACT-A new highly versatile X-Ray Spectroscopy Beamline for Catalysis and Radionuclide Science at the KIT Synchrotron Light Facility ANKA. *Rev. Sci. Instrum.* **2017**, *88* (11), No. 113113.
(43) Pandit, L.; Serrer, M.-A.; Saraçi, E.; Boubnov, A.; Grunwaldt, J.-D. Versatile in situ/operando Setup for Studying Catalysts by X-Ray Absorption Spectroscopy under Demanding and Dynamic Reaction Conditions for Energy Storage and Conversion. *Chem.: Methods* **2022**, *2* (1), No. e202100078, DOI: 10.1002/cmtd.202100078.
(44) Loewert, M.; Serrer, M.-A.; Carambia, T.; Stehle, M.; Zimina, A.; Kalz, K. F.; Lichtenberg, H.; Saraçi, E.; Pfeifer, P.; Grunwaldt, J.-D. Bridging the Gap between Industry and Synchrotron: an operando Study at 30 bar over 300 h during Fischer−Tropsch Synthesis. *React. Chem. Eng.* **2020**, *5* (6), 1071−1082.
(45) Ravel, B.; Newville, M. ATHENA, ARTEMIS, HEPHAESTUS: Data Analysis for X-Ray Absorption Spectroscopy using IFEFFIT. *J. Synchrotron Radiat.* **2005**, *12*, 537−541.
(46) Newville, M.; Livins, P.; Yacoby, Y.; Rehr, J. J.; Stern, E. A. Near-Edge X-Ray-Absorption Fine Structure of Pb: A Comparison of Theory and Experiment. *Phys. Rev. B* **1993**, *47* (21), No. 14126, DOI: 10.1103/physrevb.47.14126.
(47) Seah, M. P.; Gilmore, I. S.; Beamson, G. XPS: Binding Energy Calibration of Electron Spectrometers:Re-Evaluation of the Reference Energies. *Surf. Interface Anal.* **1998**, *26* (9), 642−649.
(48) Moulder, J.; Stickle, W.; Sobol, P.; Bomben, K. D. *Handbook of X-Ray Photoelectron Spectroscopy*; Physical Electronics, Inc., 1995.
(49) Powell, C. *X-ray Photoelectron Spectroscopy Database XPS*, Version 4.1; NIST Standard Reference Database 20.
(50) Hemming, P. E. C, H, N Micro-Analysis : a Comparative Review of the Effects of Instrument Design on Analytical Performance.
(51) Braun, E. I.; Pantano, P. The Importance of an extensive Elemental Analysis of Single-Walled Carbon Nanotube Soot. *Carbon* **2014**, *77*, 912−919.
(52) Doebelin, N.; Kleeberg, R. Profex: A Graphical User Interface for the Rietveld Refinement Program BGMN. *J. Appl. Crystallogr.* **2015**, *48* (Pt 5), 1573−1580.
(53) Thommes, M.; Kaneko, K.; Neimark, A. V.; Olivier, J. P.; Rodriguez-Reinoso, F.; Rouquerol, J.; Sing, K. S. Physisorption of Gases, with Special Reference to the Evaluation of Surface Area and Pore Size Distribution (IUPAC Technical Report). *Pure Appl. Chem.* **2015**, *87* (9−10), 1051−1069.
(54) Brunauer, S.; Emmett, P. H.; Teller, E. Adsorption of Gases in Multimolecular Layers. *J. Am. Chem. Soc.* **1938**, *60* (2), 309−319.
(55) Barrett, E. P.; Joyner, L. G.; Halenda, P. P. The Determination of Pore Volume and Area Distributions in Porous Substances. I. Computations from Nitrogen Isotherms. *J. Am. Chem. Soc.* **1951**, *73* (1), 373−380.
(56) Haiss, W.; Thanh, N. T. K.; Aveyard, J.; Fernig, D. G. Determination of Size and Concentration of Gold Nanoparticles from UV-Vis Spectra. *Anal. Chem.* **2007**, *79* (11), 4215−4221.
(57) Tarasov, A.; Schumann, J.; Girgsdies, F.; Thomas, N.; Behrens, M. Thermokinetic Investigation of binary Cu/Zn Hydroxycarbonates as Precursors for Cu/ZnO Catalysts. *Thermochim. Acta* **2014**, *591*, 1−9.
(58) Beale, A. M.; Weckhuysen, B. M. EXAFS as a Tool to interrogate the Size and Shape of mono and bimetallic Catalyst Nanoparticles. *Phys. Chem. Chem. Phys.* **2010**, *12* (21), 5562−5574.
(59) Jentys, A. Estimation of Mean Size and Shape of Small Metal Particles by EXAFS. *Phys. Chem. Chem. Phys.* **1999**, *1* (17), 4059−4063.
(60) Rodriguez, J. A.; Kim, J. Y.; Hanson, J. C.; Pérez, M.; Frenkel, A. I. Reduction of CuO in H_2: In Situ Time-Resolved XRD Studies. *Catal. Lett.* **2003**, *85* (3/4), 247−254.
(61) Słoczyn′ski, J.; Bobin′ski, W. Autocatalytic Effect in the Processes of Metal Oxide Reduction. I. Kinetic Model of the Reduction. *J. Solid State Chem.* **1991**, *92* (2), 420−435.